The high-cyclic model for sand tested beyond the usual ranges of application

L. Knittel[1] · A. Lamparter[3] · A. Niemunis[2] · H. H. Stutz[2]

Abstract

The high-cycle accumulation (HCA) model proposed by Niemunis et al. (Comput Geotech 32(4):245–263, 2005) predicts permanent deformations due cyclic loading with many small cycles (i.e. $N \geq 10^4$ cycles of strain amplitudes $\varepsilon^{\text{ampl}} \leq 10^{-3}$). In the presented tests, the pressure range p^{av} is extended from 3 to 9 bar; the influence of the void ratio $e \in (0.72, 0.95)$ and amplitudes of strains $\varepsilon^{\text{ampl}} \in (0.1\%, 1\%)$ is tested in the extended range. Some empirical HCA functions could be confirmed and some require modifications. An interesting qualitative controversy pertains to the direction of circulation in the P–Q-plane for a validation of the polarization function f_π, which does influence the rate of accumulation contrarily to the HCA assumption. The previous assumption that $\dot{\varepsilon}^{\text{acc}}$ remains constant above a certain pressure level, i.e. is independent of p^{av}, was experimentally refuted. Investigations on the cyclic preloading ($\dot{f}_N$) using 21 cyclic triaxial tests with varried monotonic strain paths between the cycle packages found a relationship of the direction of the monotonic strain path and the capacity to reduce cyclic preloading. This study's findings deepen the understanding of how cyclic preloading is reduced, but the tests also highlight the need for future research in the area.

Keywords Cyclic triaxial tests · Fine sand · High-cyclic loading · Hollow cylinder device · Local strain measurements

1 Introduction

A reliable finite element (FE) prediction of settlements and deformations demands a realistic constitutive description of the soil. For the complex condition of a high-cycle loading, the constitutive model must be covering among others the amplitude of the loads, mean pressure, average stress ratio, void ratio and the preloading history. The explicit high-cycle accumulation model (HCA model) of Niemunis et al. [26] has been proposed for this applications and used in many practical cases.

In Europe, numerous offshore wind farms will be built in the North and Baltic Seas. During their serviceability period, which is generally 25 years, offshore wind turbines (OWT) will be subjected to primarily to high cyclic wind and wave loads. For a variety of construction situations, the HCA model [12, 27, 30] was used to simulate several complicated loadings in FE calculations. A dense North Sea sand with a permeability of $k = 5 \cdot 10^{-6}$ m/s was investigated by Jostad et al. [12]. Herein, the HCA model demonstrated a reliable prognosis of the long-term deformations, also in contrast to other implicit and explicit material models.

Machaček et al. [19] used the HCA model in FE calculations to evaluate the settling behaviour of the ship lock Uelzen I, which is a well-documented geotechnical structure with long-term monitoring. The comparison of the numerical predictions with the HCA model and the field measurements can be judged as quite satisfying.

For the preliminary design of a gas turbine foundation subjected to dynamic loading, Galindo et al. [5] showed satisfactory results with the usage of the HCA model. The settlement behaviour was studied herein with a reduced

✉ L. Knittel
  lukas.knittel@outlook.de

1 Formerly at Institute of Soil Mechanics and Rock Mechanics, Keller Grundbau GmbH, Renchen, Germany

2 Institute of Soil Mechanics and Rock Mechanics, Karlsruhe Institute of Technology, Karlsruhe, Germany

3 Formerly at Institute of Soil Mechanics and Rock Mechanics, RWE Power AG, Bergheim, Germany

calibration program of the key parameters of the model. Pasten et al. [28] evaluated different accumulation functions to examine the soil response to repetitive loading. The key benefit highlighted here is the HCA model's ability to forecast accumulation as a function of cycle count, stress level, and initial density, among a selection few other constitutive models.

The HCA model is based on extensive laboratory studies on various cyclic triaxial tests under drained conditions. In this article, the HCA model is investigated beyond its usual limits of application. The rate of strain accumulation will be thoroughly investigated in an extended range its main influencing parameters. These extensions are carried out in order to be able to apply this explicit material model in an extended range of practical applications with complicated boundary conditions.

2 Symbols and notation

Herein, the stress conditions in a test are described by the average mean effective pressure p^{av} (with $p = (\sigma'_1 + 2\sigma'_3)/3$), the average deviatoric stress q^{av} (with $q = \sigma'_1 - \sigma'_3$), average stress ratio $\eta^{av} = q^{av}/p^{av}$ and deviatoric stress amplitude q^{ampl}. The isometric variables $P = \sqrt{3}p$ and $Q = \sqrt{3/2}q$ [24] are in many cases advantageous over the conventional Roscoe invariants p, q because the lengths of the stress paths and the angles between stress increments (or polarizations of amplitudes in our case) are preserved, i.e. they are the same as in the principal stress coordinate system. The axial strain ε_1 and the volumetric strain $\varepsilon_v = \varepsilon_1 + 2\varepsilon_3$ are used to calculate the lateral strain $\varepsilon_3 = (\varepsilon_v - \varepsilon_1)/2$, the deviatoric strain $\varepsilon_q = 2/3(\varepsilon_1 - \varepsilon_3)$ and the isometric strain variables $\varepsilon_P = \varepsilon_v/\sqrt{3}$ and $\varepsilon_Q = \sqrt{3/2}\varepsilon_q$. The total strain magnitude is defined as $\varepsilon = \|\boldsymbol{\varepsilon}\| = \sqrt{(\varepsilon_1)^2 + 2(\varepsilon_3)^2}$, i.e. as the Frobenius norm of the strain tensor. The above quantities can be split into a resilient = elastic = amplitude portion $\sqcup^{ampl}$ and a residual = plastic = trend = accumulated portion $\sqcup^{acc}$. The plastic strain can be measured as the irreversible deformation after a closed stress cycle. In the HCA model the plastic strain due to a single cycle is termed "the accumulation rate" (per cycle). Given the elastic stiffness, one may calculate the accumulation rate from mixed- or strain-controlled cycles too, as illustrated in [26]. In the context of the HCA model, a rate is understood as the derivative with respect to the number of cyles, $\dot{\sqcup} = \partial \sqcup / \partial N$. Normalisation is denoted by $\mathbf{A}^{\rightarrow} = \mathbf{A}/\|A\|$.

The rate of strain accumulation is described by the product

$$\dot{\boldsymbol{\varepsilon}}^{acc} = \dot{\varepsilon}^{acc}\mathbf{m} \tag{1}$$

of the scalar *intensity* $\dot{\varepsilon}^{acc} = \|\dot{\boldsymbol{\varepsilon}}^{acc}\|$ and the *direction* (a unit tensor) $\mathbf{m}$. Both, the intensity $\dot{\varepsilon}^{acc}$ and the *flow rule* $\mathbf{m}$ are empirical functions and will be presented in the next section. In the triaxial case, the flow rule can be related to the ratio $\dot{\varepsilon}_v^{acc}/\dot{\varepsilon}_q^{acc}$. The values of $\dot{\varepsilon}^{acc}$ and $\dot{\varepsilon}_v^{acc}/\dot{\varepsilon}_q^{acc}$ are measured indirectly using their time integrals.

3 Equations of the HCA model

The basic equation of the HCA model proposed by Niemunis et al. [26] reads

$$\dot{\boldsymbol{\sigma}} = \mathsf{E} : (\dot{\boldsymbol{\varepsilon}} - \dot{\boldsymbol{\varepsilon}}^{acc} - \dot{\boldsymbol{\varepsilon}}^{pl}) \tag{2}$$

with the rate $\dot{\boldsymbol{\sigma}}$ of the effective Cauchy stress $\boldsymbol{\sigma}$ (compression positive), the strain rate $\dot{\boldsymbol{\varepsilon}}$ (compression positive), the accumulation rate $\dot{\boldsymbol{\varepsilon}}^{acc}$, a plastic strain rate $\dot{\boldsymbol{\varepsilon}}^{pl}$ (necessary only for stress paths trying to surpass the yield surface). These rates are interrelated by the barotropic elastic stiffness E. Depending on the boundary conditions, Eq. (2) predicts either a change of average stress ($\dot{\boldsymbol{\sigma}} \neq \mathbf{0}$) or an accumulation of residual strain ($\dot{\boldsymbol{\varepsilon}} \neq \mathbf{0}$) or both.

For $\dot{\boldsymbol{\varepsilon}}^{acc}$ the multiplicative form Eq. (1) is used with the *flow rule* $\mathbf{m} = \dot{\boldsymbol{\varepsilon}}^{acc}/\|\dot{\boldsymbol{\varepsilon}}^{acc}\| = (\dot{\boldsymbol{\varepsilon}}^{acc})^{\rightarrow}$ (a unit tensor) and the *intensity* $\dot{\varepsilon}^{acc} = \|\dot{\boldsymbol{\varepsilon}}^{acc}\|$. Based on the test results [39, 45] which are corroborated by the literature [4, 18] the *flow rule* of the modified Cam clay (MCC) model is adopted for $\mathbf{m}$:

$$\mathbf{m} = \left[\frac{1}{3}\left(p^{av} - \frac{(q^{av})^2}{M^2 p^{av}}\right)\mathbf{1} + \frac{3}{M^2}(\boldsymbol{\sigma}^{av})^*\right]^{\rightarrow} \tag{3}$$

For the triaxial compression or extension the critical stress ratio M is

$$M_{cc} = \frac{6\sin\varphi_{cc}}{3 - \sin\varphi_{cc}} \quad \text{or} \quad M_{ec} = -\frac{6\sin\varphi_{cc}}{3 + \sin\varphi_{cc}}, \tag{4}$$

respectively. The critical friction angle φ_{cc} is slightly different from the one from monotonic triaxial tests (denoted as φ_c).

The intensity of strain accumulation $\dot{\varepsilon}^{acc}$ in Eq. (1) is calculated as a product of six functions:

$$\dot{\varepsilon}^{acc} = f_{ampl}\dot{f}_N f_e f_p f_Y f_\pi \tag{5}$$

each considering a single influencing parameter (see Table 1), i.e. the strain amplitude ε^{ampl} (function f_{ampl}), the cyclic preloading g^A ($\dot{f}_N$), void ratio e (f_e), average mean pressure p^{av} (f_p), average stress ratio η^{av} or $\bar{Y}^{av}$ (f_Y) and the effect of polarization changes ($f_\pi = 1$ for a constant polarization [40]).

Table 1 Summary of the functions and material constants of the HCA model

Function	Material constants
$f_{\text{ampl}} = \min\left\{ \left(\dfrac{\varepsilon^{\text{ampl}}}{10^{-4}}\right)^{C_{\text{ampl}}}; 10^{C_{\text{ampl}}} \right\}$	C_{ampl}
$\dot{f}_N = \dot{f}_N^A + \dot{f}_N^B$	C_{N1}, C_{N2}, C_{N3}
$\dot{f}_N^A = C_{N1} C_{N2} \exp\left[-\dfrac{g^A}{C_{N1} f_{\text{ampl}}} \right]$	C_{N1}, C_{N2}
$\dot{f}_N^B = C_{N1} C_{N3}$	C_{N1}, C_{N3}
$f_e = \dfrac{(C_e - e)^2}{1 + e} \dfrac{1 + e_{\max}}{(C_e - e_{\max})^2}$	C_e
$f_p = \exp\left[-C_p \left(\dfrac{p^{\text{av}}}{100 \text{ kPa}} - 1 \right) \right]$	C_p
$f_Y = \exp\left(C_Y \bar{Y}^{\text{av}} \right)$	C_Y
$f_\pi = 1$ for constant polarization [40]	

The normalized stress ratio $\bar{Y}^{\text{av}}$ used in f_Y is zero for isotropic stresses ($\eta^{\text{av}} = 0$) and one on the critical state line ($\eta^{\text{av}} = M_{cc}$). The function Y of Matsuoka and Nakai [20] is used for that purpose:

$$\bar{Y}^{\text{av}} = \frac{Y^{\text{av}} - 9}{Y_c - 9} \quad \text{with} \quad Y_c = \frac{9 - \sin^2 \varphi_{cc}}{1 - \sin^2 \varphi_{cc}} \quad (6)$$

$$Y^{\text{av}} = \frac{27(3 + \eta^{\text{av}})}{(3 + 2\eta^{\text{av}})(3 - \eta^{\text{av}})} \quad (7)$$

For a constant strain amplitude, the function f_N simplifies to:

$$f_N = C_{N1}[\ln(1 + C_{N2}N) + C_{N3}N] \quad (8)$$

Detailed investigations on the elastic stiffness E in Eq. (2) may be found in [42, 44]. A more general formulation for the *flow rule* **m** enabling to consider anisotropy has been published in [47]. The required material model parameters C_{ampl}, C_{N1}, C_{N2}, C_{N3}, C_e, C_p and C_Y of the remaining functions from Table 1 are determined from drained cyclic triaxial tests or correlations with grain size distribution parameters or from index tests. The large experimental effort for the calibration of the material constants of the HCA model lead to the development of a simplified calibration procedure based on correlations with the grain size distribution curve and index test results [41, 46].

4 Material and testing procedures

The drained cyclic tests have been performed in three different types of test devices, using three different sample geometries and two different saturation conditions. Full cylinder samples (diameter $d = 100$ mm, height $h = 200$ mm) with fully saturation (Fig. 1a) have been used in the tests of Sects. 5.1, 5.2 and 5.3. The tests of Sect. 5.4 have been performed in a cyclic triaxial device shown in Fig. 1b, with local measurements of deformation on cuboid-shaped samples ($a \times b = 90$ mm, $h = 180$ mm) analogous to [1, 2, 7, 9–11, 15, 16]). The cyclic variation of cell pressure, which can lead to membrane penetration effects [23, 25, 33] and other sources of errors of global deformation measurements (e.g. system compliance, bedding error), can be avoided by applying local strain measurements [15]. LDTs, i.e. strips of stainless steel equipped with strain gauges (Fig. 1b), were applied for that purpose. The cuboid-shaped samples were tested in the dry condition and without water in the pressure cell, in order to guarantee the long-term stability of the LDT measurements. The cell air pressure was kept constant to maintain a constant temperature in the cell, which is necessary for reliable LDT measurements. The cyclic variation of lateral effective stress was realized by an oscillation of pore air pressure.

In a hollow cylinder triaxial device (Fig. 1c), the tests of Sect. 5.5 were performed. The samples had an outer diameter $d_a = 100$ mm, an inner diameter $d_i = 60$ mm and a height $h = 200$ mm analogous to [3, 6, 29, 32, 49, 50]. The volume changes of both the full and the hollow cylinder samples were measured via the pore water. Thus, the samples were tested fully water-saturated. In the hollow cylinder device, an independent cyclic variation of vertical force F, torsional moment M_T, outer cell pressure p_a and inner cell pressure p_i (Fig. 1d) allows independent oscillations of three normal stresses (σ_z in vertical, σ_r in radial and σ_θ in circumferential direction) and one shear stress component $\tau_{\theta z}$. These four stresses can be converted to three principal stresses σ_1, σ_2 and σ_3 by means of a rotation of the coordinate system by the angle α. In the tests of Sect. 5.5, only the rotation $0.1° \leq \theta \leq 4.0°$ by a torsional moment M_T was applied, keeping $p_a = p_i$ constant. The problem of inhomogenes stresses σ_θ and σ_r for $p_a = p_i$ and sample slenderness for twist angles $\theta \geq 4°$ is absent in terms of element tests.

Air-pluviated samples of Karlsruhe fine sand (KFS) have been used in all tests of this series exepted of the tests in Sect. 5.5. The uniform KFS (mean grain size $d_{50} = 0.14$ mm, uniformity coefficient $C_u = d_{60}/d_{10} = 1.5$, minimum void ratio $e_{\min} = 0.677$, maximum void ratio $e_{\max} = 1.054$, grain density $\varrho_s = 2.65$ g/cm^3, subangular grain shape) has been prepared in the experiments. In Sect. 5.5 the coarser "Karlsruhe sand" (KS, mean grain size $d_{50} = 0.56$ mm, uniformity coefficient $C_u = d_{60}/d_{10} = 1.46$, minimum void ratio $e_{\min} = 0.544$, maximum void ratio $e_{\max} = 0.846$,
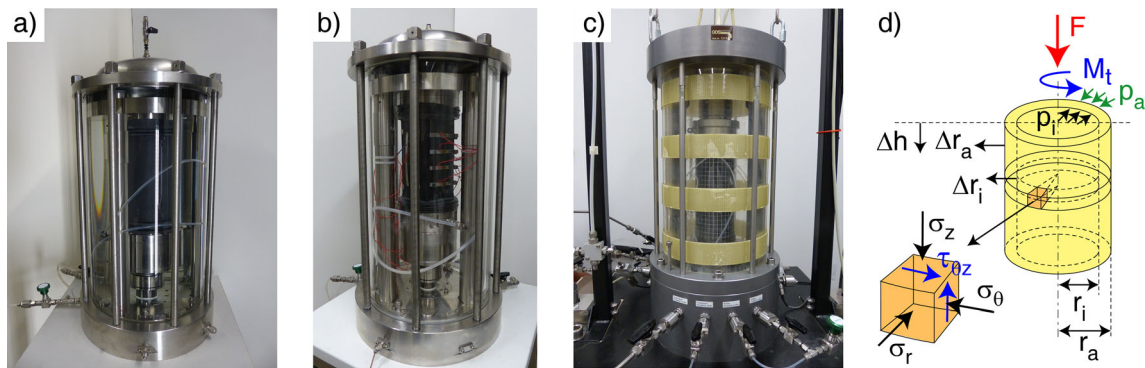
Fig. 1 Three types of devices used in the present study: (**a**) cyclic triaxial device with water-saturated full cylinder samples, (**b**) cyclic triaxial device with local strain measurements using LDTs on dry cuboid-shaped samples, (**c**) hollow cylinder device, (**d**) external loads and stresses acting on an element of soil in the hollow cylinder test [14]

grain density $\varrho_s = 2.64$ g/cm^3, subangular grain shape) was used. All tests on fully saturated samples were carried out on samples with parameters of Skempton $B = \Delta u / \Delta \sigma_3 \geq 0.98$, although for sand samples values greater than 0.97 are generally considered to be sufficiently well saturated.

5 Discussion of HCA functions

5.1 Function of cyclic preloading f_N

Tests in [17] demonstrate that the sand "remembers" its previous cyclic loading when packages of cycles are applied one after another. Similar test series could be found in the literature [8, 13, 31, 43]. Packages of cycles with different amplitudes have been applied on a compacted granite ballast in [31]. These tests proved that the final accumulated strains were independent of the order of the applied packages, analogously to the Miners's rule for fatigue [21]. The experiments confirmed the effect already observed in [48] that the monotonic loading due to the change of the average stress state erases part of the memory of the sand with respect to its cyclic preloading history, described in the HCA model by the preloading variable g^A. The reduction of g^A by a monotonic change of the mean pressure was described by a factor r, which was determined on basis of recalculations of the tests with the HCA model.

Laboratory tests in [38] presented packages of loading cycles applied on a sample of Cuxhaven sand one after another. Tests with packages of cycles with increasing loading amplitudes and constant average stress ratio η^{av} and mean pressure p^{av} were performed. The HCA model handles this load case well and reproduces the accumulation curves satisfactorily. Another test in this series with cycle packages interrupted by monotonic loading, i.e. the average stress ratio η^{av} was changed monotonically,

exposed the reduction of the cyclic preloading by monotonic strains resulting from the loading path. The average mean pressure p^{av} was constant throughout the test. The packages of cycles that follow a monotonic change of the average stress ratio η^{av} show an increased rate of strain accumulation $\dot{\varepsilon}^{acc}$. The HCA model cannot consider this effect as yet. Based on these results, the cyclic preloading g^A can be reduced or completely erased by sufficiently large monotonic straining. To study this reduction in detail, numerous laboratory investigations were carried out in the scope of this work. Their results will be described here and introduced to the HCA model.

In this section, the tests consisted of axial stress cycles. For studying the reduction of cyclic preloading, packages of cycles on different average stress states with different monotonic stress paths in the p–q-stress space were applied on the specimens. In 21 tests, 3 to 9 packages of cycles with $N = 25{,}000$ cycles and a loading frequency of $f = 0.2$ Hz were applied. All tests were evaluated regarding the accumulated strain ε^{acc} after the number of cycles N. After the evaluation, the tests were recalculated by the HCA model, wherein many tests showed the need of a reduction factor r for the cyclic preloading variable g^A by $g^A \cdot r$. This reduction factor was first introduced in [37] and has a value range of $0 \leq r \leq 1$. In this context $r = 0$ represents a complete erasing of the cyclic preloading in between the packages, whereby $r = 1$ leaves the evolution of the cyclic preloading unaffected. For a more general investigation on the reduction of cyclic preloading by monotonic deformations, the idea of applying multiple packages of cycles on different average stress states was extensively continued. Table 2 shows the variation of the tests by the different monotonic changes of the stress state between the packages. Different stress path lengths, as well contrasting path directions were tested. Figure 2 visualizes the three tests types.

Table 2 Stress paths Δp^{av}, $\Delta\eta^{av}$, resulting average strain spans $\Delta\bar\varepsilon$ and the affiliated average reduction factor $\bar r$

Δp^{av} (kPa)	$\Delta\eta^{av}$ (–)	$\Delta\bar\varepsilon$ (%)	$\bar r$ (–)	Δp^{av} (kPa)	$\Delta\eta^{av}$ (–)	$\Delta\bar\varepsilon$ (%)	$\bar r$ (–)
+ 100	–	0.08	0.9	− 100	–	0.07	0.9
+ 300	–	0.18	0.6	− 300	–	0.20	0.9
–	+ 0.25	0.40	0.3	–	− 0.25	0.09	0.9
–	+ 0.5	1.30	0.1	–	− 0.5	0.27	0.7
–	+ 1.0	1.87	0.2	–	− 1.0	0.44	0.9
− 100	+ 0.25	0.09	0.9	+ 100	− 0.25	0.12	0.9
− 100	+ 0.5	0.26	0.3	+ 100	− 0.5	0.14	1.0
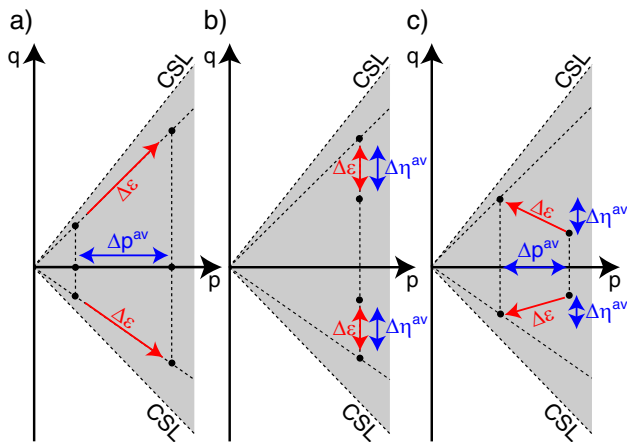
Fig. 2 Schematic stress paths: **(a)** Variation of the mean pressure interrupting cycle packages, **(b)** variation of the stress ratio interrupting the cycle packages and **(c)** simultaneous change of mean pressure and stress ratio

Changes of the effective mean pressure p^{av} are exemplarly in Fig. 2a. Table 2 matches the measured monotonic strains to the applied monotonic loading change in the p–q-space for the shown three types of tests. The overall results of the experiments carried out in this work are shown in Fig. 3, which helps to better estimate a correlation between the strain increment $\Delta\varepsilon$ arising from the monotonic stress path and the reduction factor r. The curve fitting cannot provide any firm conclusions because of the large scatter. The monotonic deviatoric loading along the critical state line (CSL) degrades the cyclic preloading faster than a simple increase of the average mean pressure, no matter if it is an increase by $\Delta p^{av} = 100$ kPa or $\Delta p^{av} = 300$ kPa which is consistent with the results presented in Table 2.

In the context of Table 2, positive $\Delta\eta$ means a change of the stress ratio leading to a stress state closer to the CSL than the stress state before (Table 2 represents compression, as well as extension tests). The mean values $\Delta\bar\varepsilon$ and $\bar r$ result from all determined values for the respective change
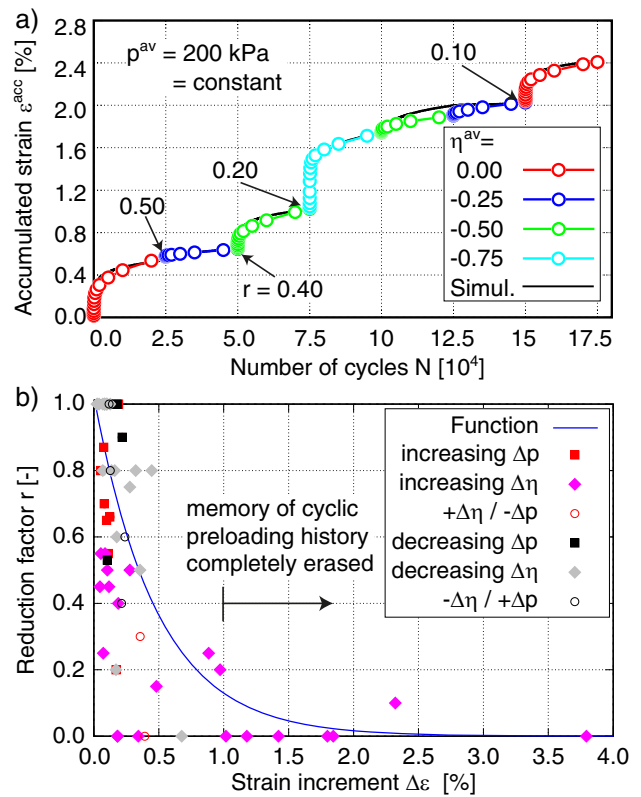

Fig. 3 **(a)** Accumulation of strain ε^{acc} in a test with experimentally change of the average stress ratio η^{av} between the cycle packages; determination of the reduction factor r from recalculation and **(b)** correlation between the monotonic strain and the reduction factor r used to find the best possible accordance of the HCA model to the test results. Extended from [35]

of the stress state. All test results in this section contribute to the understanding of the reduction of the cyclic preloading. They also show the necessity of further investigations to enable implementation of the reduction of the cyclic preloading into the HCA model.

5.2 Function of the mean pressure f_p

Investigations by Wichtmann [37] for eight different sands indicated that the barotropic function f_p could overestimate the accumulation intensity $\dot\varepsilon^{acc}$ for pressures $p^{av} \geq 300$ kPa. The pressure range investigated so far for the HCA model was 50 kPa $\leq p^{av} \leq 300$ kPa. Individual experiments suggested that $\dot\varepsilon^{acc}$ remains constant above a certain pressure level. In the triaxial devices used so far, the mean pressure $p^{av} \leq 300$ kPa could be tested at the pore (back) pressure $u = 500$ kPa, for safety reasons. For some practical applications pressures $p^{av} \geq 300$ kPa may be of interest. Therefore it should be experimentally clarified if f_p should be assumed to be constant above a certain limiting pressure.

Therefore, the testing device from Fig. 1a was equipped with an additional plexiglas cylinder, with burst protection and pressure transducers for up to 900 kPa [22]. This corresponds to an enhancement of the previous pressure range by a factor of 3. The pore (back) pressure was chosen to be $u = 500$ kPa in all tests in order to achieve a sufficient saturation. For a constant stress ratio $\eta^{av} = 0.75$ and amplitude-pressure-ratio $\varsigma = q^{ampl}/p^{av} = 0.3$ the mean pressures 200 kPa $\leq p^{av} \leq 900$ kPa were investigated. Data for smaller pressures $p^{av} \leq 150$ kPa were available from [37].

Figure 4 shows the results of the new tests for both, the accumulated strain ε^{acc} and the strain amplitude ε^{ampl} versus the number of cycles N with the exception of the experiment with $p^{av} = 500$ kPa, where the maximum density $D_{r0} = 42\%$ was present. It can be seen that the values of the strain amplitude ε^{ampl} (which is expected due to the constant amplitude-pressure relationship) as well as
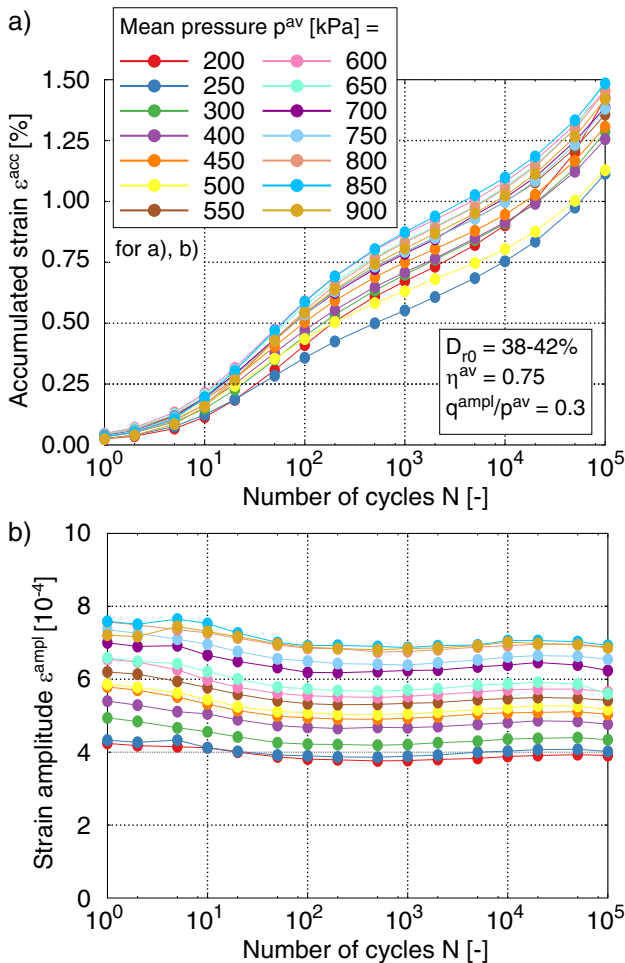
the accumulated strain ε^{acc} increase with increasing mean pressure p^{av}. Even for large pressures, an increase of the permanent deformation rate with increasing mean pressure can thus be recognized at constant ε^{ampl}. The previous assumption that $\dot{\varepsilon}^{acc}$ remains constant above a certain pressure level, i.e. is independent of p^{av}, could not be confirmed. For large pressures, a further decrease of the accumulated strain rate $\dot{\varepsilon}^{acc}$ with mean pressure can be confirmed. Thus, no changes to the pressure function f_p were necessary. The coefficient C_p corresponding to the pressure range of the respective problem may be slightly different. The parameter C_p can be determined for different numbers of cycles from the tests with different mean pressures. For this purpose, the accumulated strain after defined number of cycles N is divided by the void ratio function f_e and the amplitude function f_{ampl} of the HCA model in order to purify the test results from the influences of the different void ratios and strain amplitudes (Fig. 5). The resulting mean value of the parameter $C_p = 0.09$ determined for the pressure range $p^{av} \leq 900$ kPa is clearly smaller as the value for the pressure range 50 kPa $\leq p^{av} \leq 300$ kPa determined by Wichtmann [37] on the same sand $C_p = 0.24$ (Table 3). Here C_p represents a factor averaged according to the number of cycles analogous to [37].

5.3 Circulation changes in P–Q-plane

The circulation of cycles was claimed in [26] to be of no importance in the HCA model. This was based on multi-axial direct simple shear tests in which shearing was
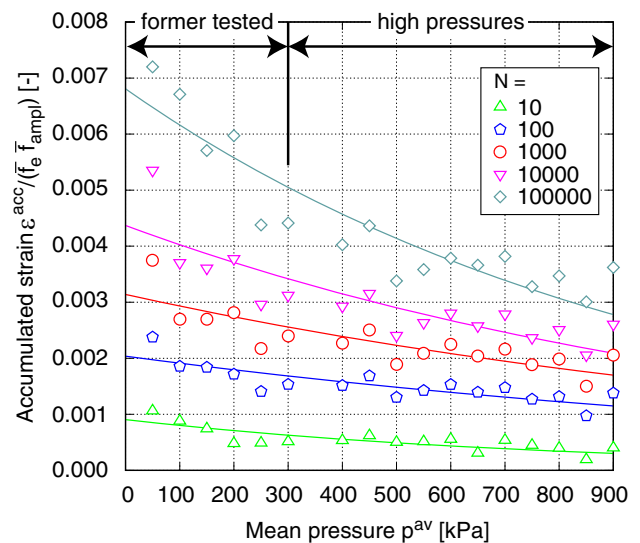

Fig. 4 Tests on samples with $38\% \leq D_{r0} \leq 42\%$ (**a**) accumulated strain ε^{acc} and (**b**) strain amplitude ε^{ampl} over number of cycles N for mean pressures $200 \leq p^{av} \leq 900$ kPa, a constant stress ratio $\eta^{av} = 0.75$ and amplitude-pressure-ratio $\varsigma = q^{ampl}/p^{av} = 0.3$

Fig. 5 Accumulated strain $\varepsilon^{acc}/(\bar{f}_e \bar{f}_{ampl})$ as a function of the mean pressure p^{av}. Investigated mean pressures 200 kPa $\leq p^{av} \leq 900$ kPa and data of former tested pressures $p^{av} \leq 150$ kPa [37]

Table 3 Parameter C_p of the pressure function of the HCA model for different numbers of cycles N

Number of cycles N	C_p
10	0.12
100	0.06
1000	0.07
10,000	0.08
100,000	0.10
Average for C_p	0.09

applied at the K_0 initial stress state. As it turned out in the present study, the circulation may significantly affect the accumulation rate. Seven different cyclic triaxial tests with relative density $D_{r0} \approx 40\%$, $N = 10^4$ cycles and circular stress paths in the P–Q-plane with a radius $r_{PQ} = 40$ kPa arround the stress state $\eta_{PQ} = Q/P = 0.24$, $P = 346$ kPa were examined. Three experiments were carried out with a counterclockwise (CCW) circulation (Fig. 6a) and three tests with clockwise (CW) circulation (Fig. 6b). The accumulated strains ε^{acc} and strain amplitudes ε^{ampl} of tests are shown in Fig. 6c, d. The difference between the direction of circulation results in 33% lower accumulated strain ε^{acc} of the CW tests than the CCW tests (Fig. 6c). For the CCW as well as CW test approximately the same strain amplitude ε^{ampl} was obtained (Fig. 6d). Some tests were repeated and turned out to be reproducible.

A seventh test (black) with similar relative density was first run for $N = 100$ cycles in CW direction (Fig. 6c, d). Then 9900 cycles followed in the CCW direction. Up to $N = 100$ cycles, the CW test are reproduced. After changing the direction of circulation, no effect on the accumulation rate can be seen. Consequently, a change in the direction of circulation leads to no change in $\dot{\varepsilon}^{acc}$.

Figure 6a, b shows graphically the explanation for the different accumulation rates of the different circulations. The stress path in the P–Q-plane was idealized as a square. The sides of the square where the path moves towards the CSL, i.e. in the direction of the flow surface, could have a decisive influence on the permanent strains. In the case of the CCW stress path, path $1 \rightarrow 2$ represents this portion (Fig. 6a), in the case of the CW stress path, path $2 \rightarrow 3$ (Fig. 6b). Presumably, path $1 \rightarrow 2$ ultimately leads to a larger accumulated strain ε^{acc} due to the larger deviatoric stress Q for $P = 346$ kPa, $\eta_{PQ} = 0.24$.

Tests with lower inclinations of the average stress state $P = 346$ kPa and $\eta_{PQ} = 0.11$, -0.11 and -0.24 are shown in Fig. 7. For $\eta_{PQ} = 0.11$ and -0.11 the accumulated strains ε^{acc} of the CW and CCW tests are almost equal (Fig. 7b, c). When applying the same stress path at $\eta_{PQ} =$
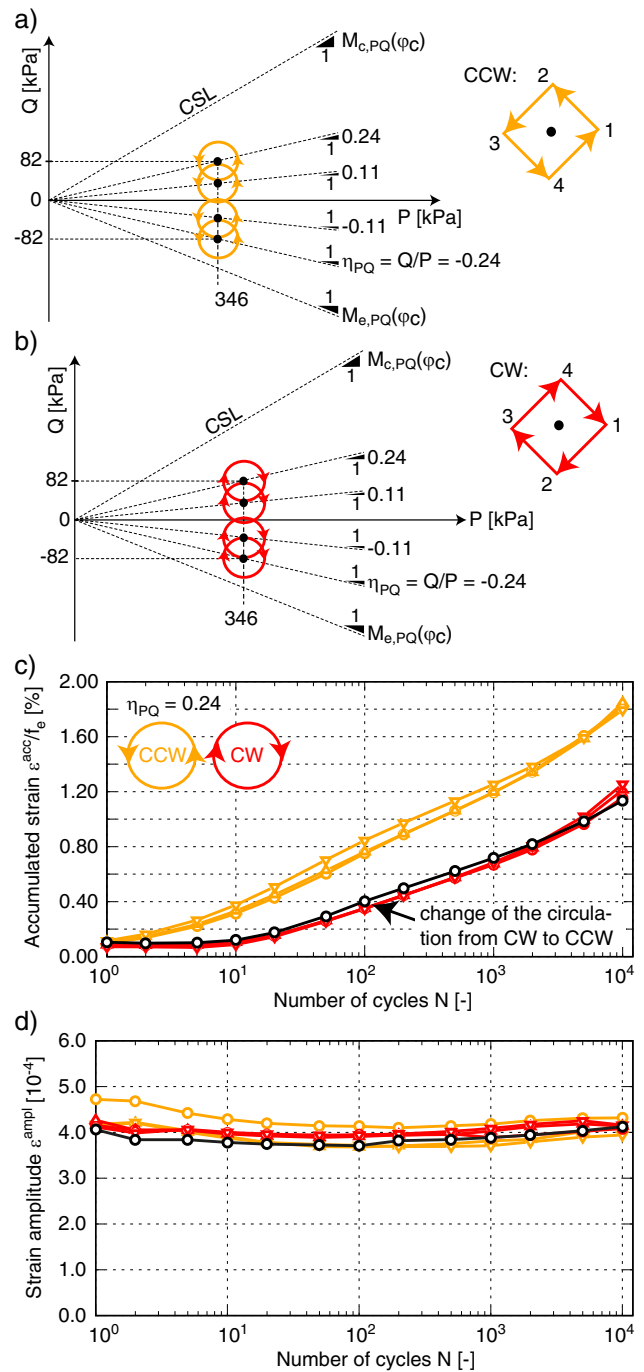
Fig. 6 Dimensional drawing of the stress path in the P–Q-plane for (**a**) counterclockwise circulation (CCW, orange) and (**b**) clockwise (CW, red) with indication of the critical state line CSL. (**c**) accumulated strains ε^{acc} and (**d**) strain amplitudes ε^{ampl} from cyclic triaxial tests on specimens with $D_{r0} \approx 40\%$ in the average stress state $\eta_{PQ} = 0.24$, $P = 346$ kPa. The seventh test (black) was first run for $N = 100$ cycles in CW and then 9900 cycles in CCW direction (color figure online)

-0.24 larger accumulated strains ε^{acc} were reached. Furthermore, a larger deformation is obtained for the CW test than for the CCW test due to the direction to the CSL.
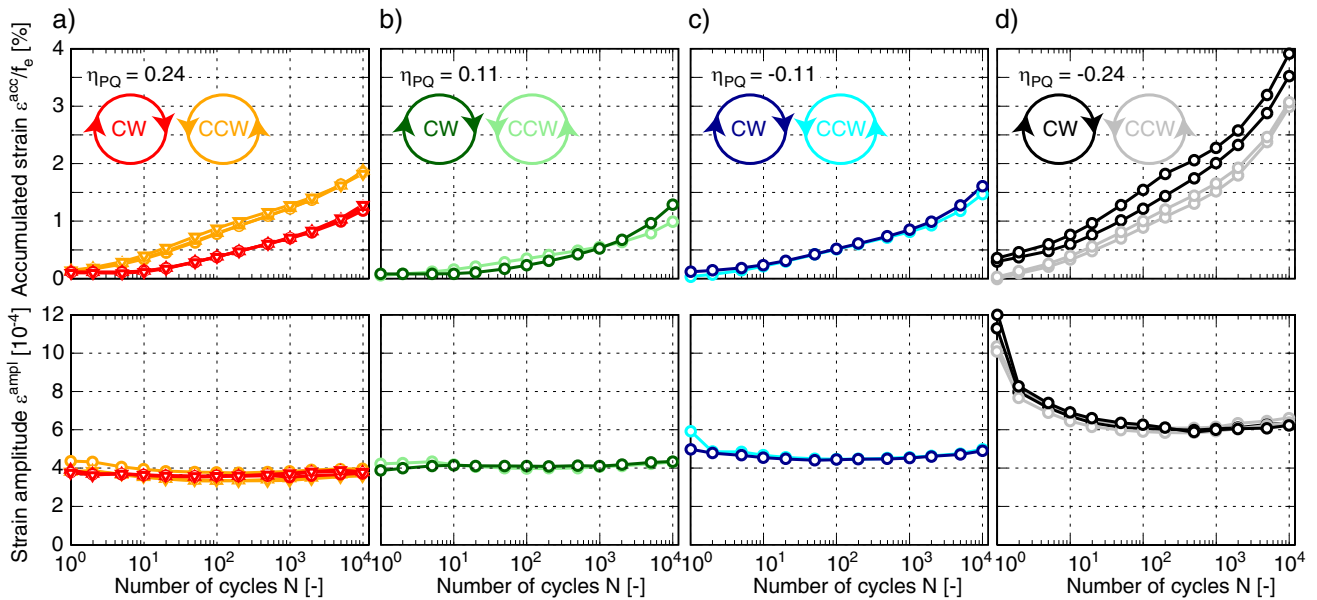
Fig. 7 Accumulated strains ε^{acc} and strain amplitudes ε^{ampl} from cyclic triaxial tests on specimens with relative density $D_r \approx 0.4$ in the average stress state **(a)** $\eta_{PQ} = 0.24$, **(b)** $\eta_{PQ} = 0.11$, **(c)** $\eta_{PQ} = -0.11$ and **(d)** $\eta_{PQ} = -0.24$ with $P = 346$ kPa

However, the HCA model has not yet included a dependence of the accumulation rate $\dot{\varepsilon}^{acc}$ on the circulation. One could try to define the circulations from Fig. 6a, b as an objective function of stress. In the space of principal (average) stresses the circulation would correspond to the rotation (a fourth-order tensor given by the Euler-Rodriguez formula) that transforms the isotropic unit compression tensor $-\vec{\delta}_{ij}$ to the direction of the average deviatoric stress $\vec{\sigma}_{ij}^*$ According to such definition, the circulations denoted as CCW (orange) are different below and above the hydrostatic axis. Analogously, the circulations denoted as CW (red) correspond to different rotations too. Judging by the results in Fig. 6b, the sense of rotation does not affect the accumulation rate. Neither the Lode angle seems to be of importance. Hence, the difference between CW (red) and CCW (orange) cycles is not a stress function. Probably, it results from an anisotropy induced by the preparation of samples. The modeling would require an additional tensorial state variable.

5.4 Function f_e of the void ratio

It has been experimentally demonstrated [37] that the reduction in the accumulation rate $\dot{\varepsilon}^{acc}$ with increasing initial relative density D_{r0} is less significant at high relative densities $D_{r0} > 80\%$. Due to the scarcity of data in this range, the function f_e was regarded for $D_{r0} > 80\%$ as uncertain. Moreover, the preparation technique could have caused a loose zone at the top of the sample with much faster accumulation. This conjecture [37] had to be verified. A series of tests were carried out, Fig. 8 to clarify this
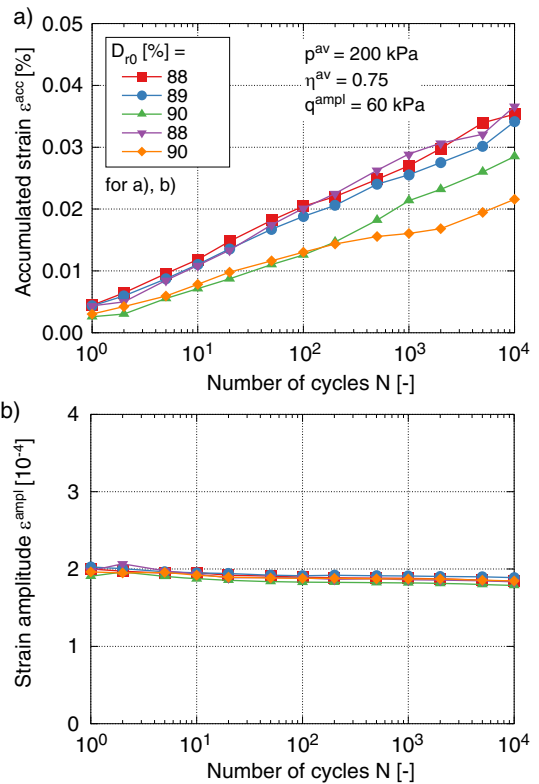

Fig. 8 Test results from specimens with relative densities $D_{r0} > 0.8$. **(a)** accumulated strain ε^{acc} and **(b)** strain amplitude ε^{ampl} over number of cycles N for an average mean pressure $p^{av} = 200$ kPa, stress ratio $\eta^{av} = 0.75$ and an applied deviatoric stress amplitude $q^{ampl} = 60$ kPa

issue [15, 34]. Five very dense samples ($D_{r0} \approx 90\%$) were tested. Global and local (LDTs) displacement measurements enabled an in-depth analysis of the deformation.

In order to reveal a possible concentration of accumulated deformations in a loosened layer at the specimens head, the deformations of the whole specimen measured outside the compression cell at the load stamp (global deformation measurement) are compared with local deformation measurements directly at the specimen. The specimens were prepared using the air pluviation method and were examined in totally dry condition. The results of all five performed experiments with a variation of the initial density $D_{r0} \approx 90\%$ is shown in Fig. 8. The curves of the accumulated strain ε^{acc} and strain amplitude ε^{ampl} over the 10,000 cycles applied are shown. The local values from the middle third of the sample confirmed the function f_e for the accumulation rate. Moreover, as expected, a slight decrease in strain amplitudes ε^{ampl} with density was observed.

The data could be well approximated by the void ratio function f_e of the HCA model. The experimental data could be fairly well fitted despite the significant curvature for $e \geq 0.85$. The parameter C_e of the void ratio function was determined to be $C_e = 0.62$ for $D_{r0} \geq 90\%$ ($e < 0.752$) with LDTs (Table 4). It differs only slightly from the model parameter $C_e = 0.60$ determined in [37] with global deformation measurement. According to [37], C_e should be averaged over the number of cycles (Fig. 9).

5.5 Function of the strain amplitude f_{ampl}

Only the tests in this section were carried out with the coarser Karlsruhe sand. Figure 10 shows the results of the hollow cylinder triaxial tests with increasing twist angle θ on samples with relative densities $44\% \leq D_{r0} \leq 84\%$. A smaller increase of the accumulated strains ε^{acc} is shown for tests with higher relative densities and lower twist angles θ. The progress of the strain amplitude ε^{ampl} is almost constant after a slight decrease. In Fig. 11 the residual strain is plotted as a function of the strain amplitude ε^{ampl}. The values of ε^{acc} were normalized with f_e in order to consider the influences of the void ratio. It is

Table 4 Parameter C_e of the void ratio function of the HCA model for different numbers of cycles N

Number of cycles N	C_e
10	0.615
100	0.636
1000	0.643
10,000	0.637
Average for C_e	0.624
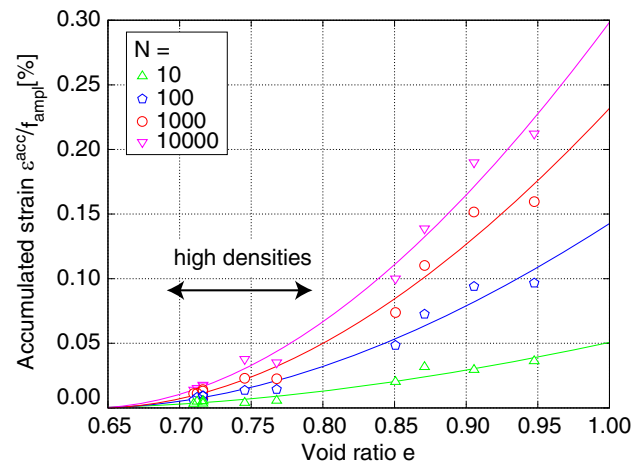
Fig. 9 Accumulated strain (and amplitude-purified) $\varepsilon^{acc}/\bar{f}_{ampl}$ as a function of e and values of the parameter C_e of the function of void ratio from the HCA model for different numbers of cycles N

obvious that the relationship $\varepsilon^{acc} \sim (\varepsilon^{ampl})^2$ loses its validity for large strain amplitudes (starting from approx. $\varepsilon^{ampl} = 10^{-3}$) as already mentioned in [36]. Thus, these experiments in the hollow cylinder device confirm the previous observations for an extended strain range up to $\varepsilon^{ampl} \leq 10^{-2}$.

6 Summary and conclusions

This study discusses five of the six HCA model functions. A factor of three was added to the prior pressure range, increasing it to $p^{av} \leq 900$ kPa. The experiments revealed that even under high pressures, the permanent deformations increased as mean pressure increased. Therefore, if the calculated pressure parameter C_p is used at high pressure (300 kPa $\leq p^{av} \leq 900$ kPa), no improvement to the current pressure function f_p is required. As a result, the HCA model's applicability might be further increased to high pressure levels for a wider variety of applications. The validation of relative densities $D_{r0} \approx 90\%$, revealed a decline in the accumulation intensity, $\dot{\varepsilon}^{acc}$. Additionally, these studies demonstrate that strain amplitudes ε^{ampl} do indeed somewhat decrease even for high initial densities. In studies on the cyclic preloading ($\dot{f}_N$), a further analysis employing 21 cyclic triaxial tests with various monotonic strain paths between the cycle packages discovered a link between the direction of the monotonic strain path and the ability to reduce cyclic preloading. The results of this study add to the understanding of how cyclic preloading is decreased, but the tests also demonstrate the need for more investigation in this area.

Circulation changes in the P–Q-plane for a validation of the polarization function f_π showed a dependence of the
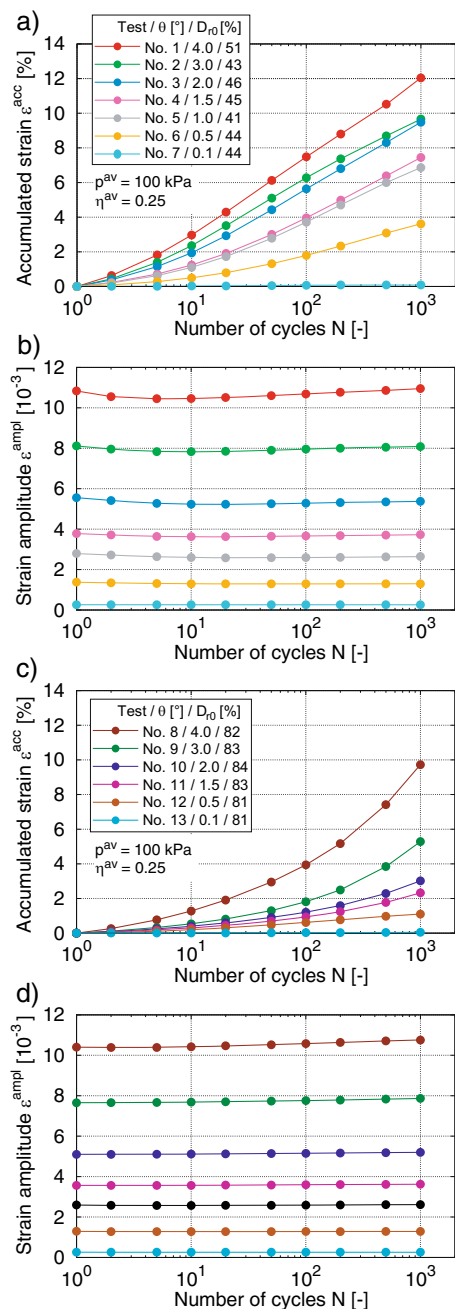
Fig. 10 Comparison of accumulated strain ε^{acc}/f_e and total strain amplitude ε^{ampl} for different torsion angles $0.1 \leq \theta \leq 4°$ and relative densities after the first irregular cycle. (**a, b**) $D_{r0} \approx 50\%$ and (**c, d**) $D_{r0} \approx 80\%$ on hollow cylinder samples of coarse grained Karlsruhe sand

Fig. 11 Accumulated strain ε^{acc}/f_e as a function of ε^{ampl} from Fig. 10 for numbers of cycles $N = 20$, 100 and 1000

References

1. AnhDan L, Koseki J (2004) Effects of large number of cyclic loading on deformation characteristics of dense granular materials. Soils Found 44(3):115–123
2. AnhDan L, Koseki J, Sato T (2002) Comparison of Young's moduli of dense sand and gravel measured by dynamic and static methods. Geotech Test J ASTM 25(4):349–358
3. Baziar MH, Sharafi H (2011) Assessment of silty sand liquefaction potential using hollow torsional tests—an energy approach. Soil Dyn Earthq Eng 31:857–865
4. Chang CS, Whitman RV (1988) Drained permanent deformation of sand due to cyclic loading. J Geotech Eng ASCE 114(10):1164–1180
5. Galindo R, Illueca M, Jimenez R (2014) Permanent deformation estimates of dynamic equipment foundations: application to a gas turbine in granular soils. Soil Dyn Earthq Eng 63(1):8–18
6. Georgiannou VN, Tsomokos A (2008) Comparison of two fine sands under torsional loading. Can Geotech J 45:1659–1672

direction of rotation on the stress state in both the compression and extension area. This dependence is currently not considered in the HCA model. Investigations with large strain amplitudes $10^{-4} \leq \varepsilon^{ampl} \leq 10^{-2}$ in the hollow cylinder triaxial device confirmed the limitation of the strain amplitude of $\varepsilon^{ampl} = 10^{-3}$ in the HCA model.

7. Goto S, Tatsuoka F, Shibuya S, Kim Y-S, Sato T (1991) A simple gauge for local small strain measurements in the laboratory. Soils Found 31(1):169–180

8. Guan QZ, Yang ZX (2023) Hybrid deep learning model for prediction of monotonic and cyclic responses of sand. Acta Geotech 18:1447–1461

9. Hoque E, Sato T, Tatsuoka F (1997) Performance evaluation of LDTs for use in triaxial tests. Geotech Test J 20(2):149–167

10. Hoque E, Tatsuoka F (1998) Anisotropy in elastic deformation of granular materials. Soils Found 38(1):163–179

11. Hoque E, Tatsuoka F (2004) Effects of stress ratio on small-strain stiffness during triaxial shearing. Géotechnique 54(7):429–439

12. Jostad HP, Dahl BM, Page A, Sivasithamparam N, Sturm H (2020) Evaluation of soil models for improved design of offshore wind turbine foundations in dense sand. Géotechnique 70(8):682–699

13. Kaggwa WS, Booker JR, Carter JP (1991) Residual strains in calcareous sand due to irregular cyclic loading. J Geotech Eng ASCE 117(2):201–218

14. Knittel L (2020) Granular soils under multidimensional cyclic loading. Dissertation, Institute for Soil Mechanics and Rock Mechanics, Karlsruhe Institute of Technology (KIT), No. 188

15. Knittel L, Wichtmann T, Niemunis A, Huber G, Espino E, Triantafyllidis T (2020) Pure elastic stiffness of sand represented by response envelopes derived from cyclic triaxial tests with local strain measurements. Acta Geotech 15:2075–2088

16. Lenart S, Koseki J, Miyashita Y, Sato T (2014) Large-scale triaxial tests of dense gravel material at low confining pressures. Soils Found 54(1):45–55

17. López-Querol S, Bázquez R (2007) Validation of a new endochronic liquefaction model for granular soil by using centrifuge test data. Soil Dyn Earthq Eng 27(2):920–937

18. Luong MP (1982) Mechanical aspects and thermal effects of cohesionless soils under cyclic and transient loading. In: Proc. IUTAM Conf. on deformation and failure of granular materials, Delft, pp 239–246

19. Machaček J, Wichtmann T, Zachert H, Triantafyllidis Th (2018) Long-term settlements of a ship lock: measurements vs. FE-prediction using a high cycle accumulation model. Comput Geotech 97(5):222–232

20. Matsuoka H, Nakai T (1982) A new failure criterion for soils in three-dimensional stresses. In: Proc. IUTAM Symp. in Delft. Deformation and failure of granular materials, pp 253–263

21. Miner M (1945) Cumulative damage in fatigue. Trans Am Soc Mech Eng 67:A159–A164

22. Munoz Rodriguez PC (2019) Investigations on the strain accumulation of sand under cyclic loading with high pressures and large stress amplitudes. Bachelorarbeit. Institut für Bodenmechanik und Felsmechanik, Karlsruher Institut für Technologie (KIT), 9

23. Nicholson PG, Seed RB, Anwar HA (1993) Elimination of membrane compliance in undrained triaxial testing. I. Measurement and evaluation. Can Geotech J 30(5):727–738

24. Niemunis A (2003) Extended hypoplastic models for soils. Habilitation, Veröffentlichungen des Institutes für Grundbau und Bodenmechanik, Ruhr-Universität Bochum, Heft Nr. 34

25. Niemunis A, Knittel L (2020) Removal of the membrane penetration error from triaxial data. Open Geomech 2(5)

26. Niemunis A, Wichtmann T, Triantafyllidis Th (2005) A high-cycle accumulation model for sand. Comput Geotech 32(4):245–263

27. Page, AM, Klinkvort RT, Bayton S, Zhang Y, Jostad HP A procedure for predicting the permanent rotation of monopiles in sand supporting offshore wind turbines. Mar Struct

28. Pasten C, Shin H, Santamarina JC (2014) Long-term foundation response to repetitive loading. J Geotech Geoenviron Eng ASCE 140(4)

29. Shahnazari H, Towhata I (2002) Torsion shear tests on cyclic stress-dilatancy relationship of sand. Soils Found 42(1):105–119

30. Staubach P, Wichtmann T (2020) Long-term deformations of monopile foundations for offshore wind turbines studied with a high-cycle accumulation model. Comput Geotech 124

31. Stewart HE (1986) Permanent strains from cyclic variable-amplitude loadings. J Geotech Eng ASCE 112(6):646–660

32. Tatsuoka F, Ochi K, Fujii S, Okamoto M (1986) Cyclic undrained triaxial and torsional shear strength of sands for different sample preparation methods. Soils Found 26(3):23–41

33. Tokimatsu K (1990) System compliance correction from pore pressure response in undrained triaxial tests. Soils Found 30(2):14–22

34. Wappler A (2019) Verformungsakkumulation in dichtest gelagertem Sand unter zyklischer Beanspruchung, Bachelorarbeit. Institut für Bodenmechanik und Felsmechanik, Karlsruher Institut für Technologie (KIT), 1

35. Wappler A, Knittel L, Niemunis A, Stutz HH (2022) On the erasing of the cyclic history by monotonic deformations. In: 41st International conference on ocean, offshore and arctic engineering (OMAE), Hamburg

36. Wichtmann T (2005) Explicit accumulation model for non-cohesive soils under cyclic loading. PhD thesis, Publications of the Institute of Soil Mechanics and Foundation Engineering, Ruhr-University Bochum, Issue No. 38

37. Wichtmann T (2016) Soil behaviour under cyclic loading—experimental observations, constitutive description and applications. Habilitation thesis, Publications of the Institute of Soil Mechanics and Rock Mechanics, Karlsruhe Institute of Technology, No. 181

38. Wichtmann T, Knittel L (2019) Behaviour of granular soils under uni- and multidimensional drained high-cyclic loading. In: Triantafyllidis Th (ed) Recent developments of soil mechanics and geotechnics in theory and practice. Springer, Berlin, pp 136–165

39. Wichtmann T, Niemunis A, Triantafyllidis Th (2006) Experimental evidence of a unique flow rule of non-cohesive soils under high-cyclic loading. Acta Geotech 1(1):59–73

40. Wichtmann T, Niemunis A, Triantafyllidis Th (2007) On the influence of the polarization and the shape of the strain loop on strain accumulation in sand under high-cyclic loading. Soil Dyn Earthq Eng 27(1):14–28

41. Wichtmann T, Niemunis A, Triantafyllidis Th (2009) Validation and calibration of a high-cycle accumulation model based on cyclic triaxial tests on eight sands. Soils Found 49(5):711–728

42. Wichtmann T, Niemunis A, Triantafyllidis Th (2010) On the elastic stiffness in a high-cycle accumulation model for sand: a comparison of drained and undrained cyclic triaxial tests. Can Geotech J 47(7):791–805

43. Wichtmann T, Niemunis A, Triantafyllidis Th (2010) Strain accumulation in sand due to drained cyclic loading: on the effect of monotonic and cyclic preloading (Miner's rule). Soil Dyn Earthq Eng 30(8):736–745

44. Wichtmann T, Niemunis A, Triantafyllidis Th (2013) On the elastic stiffness in a high-cycle accumulation model—continued investigations. Can Geotech J 50(12):1260–1272

45. Wichtmann T, Niemunis A, Triantafyllidis Th (2014) Flow rule in a high-cycle accumulation model backed by cyclic test data of 22 sands. Acta Geotech 9(4):695–709

46. Wichtmann T, Niemunis A, Triantafyllidis Th (2015) Improved simplified calibration procedure for a high-cycle accumulation model. Soil Dyn Earthq Eng 70(3):118–132

47. Wichtmann T, Rondón HA, Niemunis A, Triantafyllidis Th, Lizcano A (2010) Prediction of permanent deformations in

pavements using a high-cycle accumulation model. J Geotech Geoenviron Eng ASCE 136(5):728–740

48. Wichtmann T, Triantafyllidis Th (2017) Strain accumulation due to packages of cycles with varying amplitude and/or average stress—on the bundling of cycles and the loss of the cyclic preloading memory. Soil Dyn Earthq Eng 101:250–263

49. Yamashita S, Toki S (1993) Effects of fabric anisotropy of sand on cyclic undrained triaxial and torsional strengths. Soils Found 33(3):92–104

50. Yoshimine M, Ishihara K, Vargas W (1998) Effects of principle stress direction and intermediate principle stress on undrained shear behavior of sand. Soils Found 38(3):179–188

Publisher's Note Springer Nature remains neutral with regard to jurisdictional claims in published maps and institutional affiliations.